

To appear in *The Astronomical Journal*

Neutral Gas Distribution and Kinematics of the Nearly Face-on Spiral Galaxy NGC 1232

Liese van Zee¹

National Radio Astronomy Observatory,² PO Box 0, Socorro, NM 87801
lvanee@nrao.edu

Jessica Bryant

Agnes Scott College, Decatur, GA 30030
jbryant@agnesscott.edu

ABSTRACT

We have analyzed high velocity resolution HI synthesis observations of the nearly face-on Sc galaxy NGC 1232. The neutral gas distribution extends well beyond the optical extent of the galaxy. As expected, local peaks in the HI column density are associated with the spiral arms. Further, the HI column density drops precipitously near the center of the galaxy. Closed contours in the velocity field suggest either that the system is warped, or that the rotation curve declines. The velocity dispersion is approximately constant throughout the system, with a median value of 9.9 ± 1.8 km s⁻¹. When corrected for rotational broadening, there is no indication of a radial trend in the neutral gas velocity dispersion in this galaxy.

Subject headings: galaxies: abundances — galaxies: individual (N1232, N1232A) — galaxies: kinematics and dynamics — galaxies: spiral

1. Introduction

NGC 1232 is a nearly face-on, gas-rich, Sc galaxy. Face-on galaxies provide excellent targets for studies of radial properties, such as the chemical enrichment of the interstellar medium (e.g., McCall, Rybski, & Shields 1985; Vila-Costas & Edmunds 1992; Zaritsky, Kennicutt, & Huchra

¹Jansky Fellow

²The National Radio Astronomy Observatory is a facility of the National Science Foundation, operated under a cooperative agreement by Associated Universities Inc.

1994; Ferguson, Gallagher, & Wyse 1998) or the velocity dispersion of the neutral gas (e.g., van der Kruit & Shostak 1982, 1984; Shostak & van der Kruit 1984; Dickey, Hanson, & Helou 1990; Boulanger & Viallefond 1992; Kamphuis & Briggs 1992; Rownd, Dickey, & Helou 1994). NGC 1232 first came to our attention as part of a study of radial trends in elemental abundances (van Zee, Salzer, & Haynes 1998a; van Zee *et al.* 1998b). The outermost H II region observed by van Zee *et al.* (1998a,b) has an abnormally low oxygen abundance and a higher N/O ratio than expected at that radius. Such features may arise from asymmetries in the disk, or from perturbations induced by tidal interactions. We thus decided to investigate the neutral gas distribution and kinematics of NGC 1232 to determine if there were kinematic peculiarities associated with this particular H II region, or more generally in the outer gas disk.

With a relatively low inclination angle, approximately 30° , NGC 1232 is also a prime candidate for studies of the neutral gas velocity dispersion as a function of radius. Since the HI distribution typically extends a factor of 1.3 to 2 times the size of the optical disk in Sc galaxies (e.g., Broeils & Rhee 1997), one might naively expect a decrease in the observed velocity dispersion beyond the radius of active star formation [star formation activity may not be truncated in spiral galaxies, however (Ferguson *et al.* 1998b)]. Previous studies of the neutral gas velocity dispersion in face-on spiral galaxies have been inconclusive. While some observations indicate that the velocity dispersion may decrease with radius (e.g., NGC 6946, Boulanger & Viallefond 1992), others indicate that the velocity dispersion is constant in the outer gas disk (e.g., NGC 1058, Dickey *et al.* 1990). Such studies are hampered by two main problems: (1) rotational broadening and (2) insufficient spectral resolution. The observations of NGC 1232 presented in this paper have adequate spectral resolution, but suffer from significant rotational broadening, in part due to a severe warp in the gas disk. Nonetheless, these observations do provide additional insight on radial trends of the neutral gas velocity dispersion in spiral galaxies.

The physical parameters of NGC 1232 are summarized in Table 1. Throughout this paper, we adopt a distance of 21.5 Mpc (van Zee *et al.* 1998b), based on an assumed H_0 of $75 \text{ km s}^{-1} \text{ Mpc}^{-1}$ and a Virgocentric infall model. Optically, NGC 1232 is a rather nondescript Sc galaxy with well defined spiral arms and optical colors (de Vaucouleurs *et al.* 1991) that are typical for late-type spiral galaxies. Its total HI mass and $M_{\text{HI}}/L_{\text{B}}$ ratio are also quite typical of the class. On the other hand, its far infrared luminosity (Soifer *et al.* 1989) is significantly lower than typical for Sc galaxies (see, e.g., Roberts & Haynes 1994 for trends as a function of Hubble type).

This paper is organized as follows. The HI synthesis observations and data reduction are presented in Section 2. The neutral gas distribution and kinematics of NGC 1232 are discussed in Section 3. A brief discussion and summary are presented in Sections 4 and 5. Finally, the results of optical spectroscopy of the spatially nearby system NGC 1232A are summarized in an appendix.

2. Observations and Data Reduction

HI synthesis imaging observations of NGC 1232 were conducted by the NRAO summer students with the DnC configuration of the Very Large Array³ (VLA) on 1992 July 4. The observations spanned 5 hours, with a total on–source integration time of 227 minutes. The correlator was used in 2AD mode with the right and left circular polarizations tuned to 1684 km s^{−1}. The total band width was 1.56 MHz. The on–line Hanning smoothing option was selected, producing final spectral data cubes of 127 channels, each 2.6 km s^{−1} wide. Standard tasks in AIPS (Napier *et al.* 1983) were employed for calibration and preliminary data reduction. Calibration of this data set was complicated by the fact that the west arm of the array was shadowed during the observations of the primary flux density calibrator, 3C 286. However, the observations of 3C 286 were sufficient to set the flux density scale; phase and bandpass calibration was derived from observations of a nearby continuum source, B0237–233. With an observed flux density of 6.21 Jy at 1412.5 MHz, the observations of B0237–233 had adequate signal–to–noise for calibration of both the phase and the bandpass.

After calibration, the line data was transformed to the x – y plane. A robust weighting technique was employed by the AIPS task IMAGR to optimize the beam shape and noise levels of the final data cubes (Briggs 1995). The “robustness parameter” in IMAGR controls the weighting of the u – v data, permitting a fine–tuning between sensitivity and resolution. As currently implemented, a robustness of 5 corresponds to natural weighting of the u – v data (maximizing sensitivity) while a robustness of −5 corresponds to uniform weighting (lower sensitivity, but better spatial resolution). The relevant IMAGR parameters for three data cubes are listed in Table 2. Throughout this paper we will refer to the robustness of 1.0 cube as the “low resolution cube,” to the robustness of 0.5 cube as the “intermediate weight cube,” and to the robustness of −0.5 cube as the “high resolution cube.” All subsequent analysis of the data cubes was performed within the GIPSY package (van der Hulst *et al.* 1992).

Line emission from NGC 1232 filled most of the bandpass (channels 7 to 121). Since the few line–free channels were at the extreme edge of the bandpass, they had poor noise characteristics and thus were insufficient to create an accurate model of the continuum emission in either the u – v or x – y planes. Continuum subtraction was a necessary step in the data reduction process, however, since NGC 1232 has 58.5 mJy of continuum emission at L–band (Condon 1987). Continuum subtraction was conducted in the x – y plane, with a continuum image created separately for each data cube. To create the continuum image, the mean of the inner 100 channels ($1553.8 < v < 1814.3$ km s^{−1}) was computed. This image was severely contaminated by the line emission of the galaxy; the region of galaxy emission was blotted from the image and replaced with the value 0. Next, the mean was computed for channels with velocities between 1538.2 and 1561.6 km s^{−1} (line emission from only the eastern half of the galaxy) and for channels with velocities

³The Very Large Array is a facility of the National Radio Astronomy Observatory.

between 1811.7 and 1835.2 km s⁻¹ (line emission from only the western half of the galaxy). The continuum sources coincident with the galaxy emission were recovered from these two maps. The final continuum image for each resolution was inspected to verify that all of the continuum sources were recovered; an example of one of these continuum images (from the intermediate weight data cube) is shown in Figure 1.

The continuum image for each resolution was subtracted from every channel of the data cube to produce the final continuum-free data cubes. Selected channels from the continuum subtracted intermediate weight data cube are presented in Figure 2. The continuum subtraction appears to have been successful (see, for instance, the baseline of the integrated flux density profile, Figure 3). Note, however, that even if the continuum subtraction had not been as successful, the subsequent analysis of the gas kinematics and dynamics would still be valid. In particular, the velocity field and velocity dispersion measurements are fairly robust, even in the presence of continuum emission; only the total gas distribution would have been significantly effected by poor continuum subtraction.

To determine if the total HI flux density was recovered in the HI synthesis observations, the flux density was measured in each channel of the continuum subtracted data cubes. The flux density profile, corrected for primary beam attenuation, is shown in Figure 3. Qualitatively, the flux density profile is similar to those obtained from single dish observations (Fisher & Tully 1981; Reif *et al.* 1982; Staveley-Smith & Davies 1988). The total flux density recovered from the low resolution data cube was 122.4 ± 12.2 Jy km s⁻¹, in good agreement with previous single dish measurements (e.g., 115.5 ± 7.2 Jy km s⁻¹, Green Bank 43m [Fisher & Tully 1981]; 127.9 ± 13.8 Jy km s⁻¹, Jodrell Bank [Staveley-Smith & Davies 1988]). Thus, despite the calibration problems and missing short spacings, the flux density scale appears to be correct, and the total HI flux density has been recovered.

The slight asymmetry between the two horns of the integrated HI profile has been ascribed to emission from the spatially nearby galaxy NGC 1232A (ESO 547-G016) (e.g., Reif *et al.* 1982; Becker *et al.* 1988). However, there is no apparent gas density enhancement or perturbation in the velocity field near this object (see Figure 4). Furthermore, a heliocentric optical velocity of $6570. \pm 15.$ km s⁻¹ was measured from several emission lines with the Palomar 5m telescope;⁴ further details of the emission lines observed in this galaxy are presented in the appendix. This newly derived redshift is in basic agreement with the velocity listed in NED;⁵ thus, this object does not appear to be physically associated with NGC 1232.

Both moment analysis and Gaussian fitting were used to characterize the gas distribution,

⁴Observations at the Palomar Observatory were made as part of a continuing cooperative agreement between Cornell University and the California Institute of Technology.

⁵The NASA/IPAC Extragalactic Database (NED) is operated by the Jet Propulsion Laboratory, California Institute of Technology, under contract with the National Aeronautics and Space Administration.

velocity field, and velocity dispersion of NGC 1232. Moment maps of each data cube were computed in the following manner. First, the low resolution cube was smoothed to a resolution of twice the beam; second, the smoothed cube was clipped at the 2σ level; the resultant clipped cube was then interactively blanked to remove spurious noise spikes. Signal was identified based on spatial continuity between channels. A conditional transfer was used to blank the corresponding locations in the low, intermediate, and high resolution data cubes (corrected for primary beam attenuation) based on the blanked, smoothed cube. Moment maps of the blanked data cubes were created with the GIPSY task MOMENTS. In addition, Gaussian fits to the observed line profiles at each position in the unclipped data cubes were obtained with the GIPSY task GAUFIT. In regions of high signal-to-noise, Gaussian fitting is preferred over moment analysis since it is less susceptible to beam smearing. The resultant maps were qualitatively similar to the moment maps in both gas distribution and velocity field. However, significant differences were found in the velocity dispersion maps, probably due to beam smearing. Thus, the moment maps were used for investigation of the gas distribution and kinematics, while interactive Gaussian fitting was employed for study of the velocity dispersion as a function of position. The zeroth and first moments are presented in Figure 4; the optical images used in this figure are described more fully in van Zee *et al.* (1998b).

3. Analysis

3.1. Gas Distribution and Velocity Field

There are several notable features in the gas distribution of NGC 1232. First, the HI distribution extends well beyond the optical radius. At a column density limit of 10^{20} atoms cm^{-2} , the HI-to-optical diameter ratio is 1.6, quite typical of spiral galaxies (e.g., Cayatte *et al.* 1994; Broeils & Rhee 1997). Second, as has been seen in many other massive galaxies (e.g., Brinks & Bajaja 1986; Broeils & van Woerden 1994), the neutral gas column density is lower in the center of the galaxy. The azimuthally averaged radial profile of the gas density is shown in Figure 5d and tabulated in Table 3. As seen in Figure 5d, the eastern and western sides of the galaxy are not perfectly symmetric. The eastern half of the galaxy has a higher column density, corresponding to the prominent spiral arms on that side. On the western side, the gas distribution extends to larger radii, perhaps due to a warp of the gas disk in the outer regions. The observed asymmetry between the horns of the global HI profile is the result of the convolution of this asymmetric gas distribution with the rotation of the disk. Such asymmetries are not expected to be long lived, but also are not uncommon in spiral galaxies (e.g., Haynes *et al.* 1998).

Closed contours in the velocity field (Figure 4d) suggest that the outer gas disk is warped, causing an apparent decline in the rotation curve. A model for the rotation curve of NGC 1232 was derived using tilted-ring analysis of the intermediate resolution velocity field. The process of fitting a rotation curve is iterative; we began by fitting both sides of the velocity field in order to

determine the kinematic center and systemic velocity (Table 1). Next, the center and systemic velocity were held fixed and each side was fit separately to determine the position and inclination angles. The position angle was well constrained by the models. However, the fit to the inclination angle was relatively unconstrained. Based on the optical axial ratios, the inclination angle was initially assumed to be approximately 30° . Since the ROTCUR fits resulted in wild variations of the inclination angle, the inclination was set to 30° in the inner regions of the galaxy and then permitted to slowly decrease in the outer regions. Finally, the rotation curve for each side was determined by fixing the inclination and position angles to the average of both sides with the additional constraint that these values must change smoothly from ring to ring. The result of ROTCUR’s fit to the approaching and receding sides are shown in Figure 5; Table 3 lists the average values for both sides. As seen in the upper panel of Figure 5, a warped disk model is able to recover a flat rotation curve in the outer gas disk. However, since the inclination angle was poorly constrained by the tilted–ring models, we cannot rule out the possibility that the inclination angle is constant at all radii (i.e., the gas disk may not be warped). Thus, a rotation curve was also derived using the same parameters as the warped disk model, with the exception that the inclination angle was held fixed at 30° throughout the disk; not unexpectedly, this model results in a falling rotation curve in the outer disk.

Figure 6 shows the position–velocity diagram for a slice along the major axis of NGC 1232. The rotation curve derived from the warped disk model is superposed. As frequently found in spiral galaxies, the warp appears to begin at the edge of the optical disk (see e.g., NGC 4013, Sparke & Casertano 1988; NGC 4138, Jore, Broeils, & Haynes 1996).

Both the warped disk and falling rotation curve models adequately reproduce the major features of the velocity field. However, several kinks in the iso–velocity contours are found in the outer regions of the gas disk which cannot be well fit by either of these models. Such kinks are usually associated with spiral streaming motions, but these features occur in regions well beyond the prominent spiral arms. Note, however, that such features would be difficult to detect in the inner regions due to the presence of a steeply rising rotation curve. Thus, their apparent absence in the inner region of the galaxy does not eliminate the possibility that they arise from the continuation of spiral density waves to the edge of the disk. Due to the steep rotational gradient, higher spatial resolution observations will be needed to investigate fully the pattern speeds in the outer gas disk.

3.2. Rotation Curve Analysis

The derived rotation curves were used to determine the dark matter content of NGC 1232. Rotation curve decomposition requires knowledge of the gaseous and stellar mass distributions (assumed to be disk–like) and an assumed dark matter distribution. The contribution of the gaseous and stellar components to the gravitational potential were calculated using the GIPSY routine ROTMOD. The input surface densities were estimated from a series of ellipses with position

angles of 270° and inclinations of 30° . The stellar distribution was taken as the observed azimuthal average to the extent of the optical emission (Figure 5e), followed by an extrapolated exponential disk. In fitting the rotation curve, the HI distribution was multiplied by $4/3$ to account for the He content. The gas content was held fixed during the fitting process. Note that for the observed neutral gas distribution of NGC 1232, the net acceleration is outwards for the inner part of the gas disk; following the usual convention, this outward acceleration is denoted by a negative velocity. The stellar disk was fit with one free parameter, the mass-to-light ratio (M/L_B). Note that since the available R-band image was obtained under non-photometric conditions, the observed surface brightness distribution was scaled to match the total blue luminosity (de Vaucouleurs *et al.* 1991). While B-band and R-band scale lengths are typically slightly different for spiral galaxies (see, e.g., de Jong 1996), this minor difference should be insignificant for the present mass models. A simple spherical halo model was used for the dark matter contribution; this model has only two free parameters, the core radius, R_c , and the central density, ρ_o :

$$\rho(r) = \rho_o \left(1 + \left(\frac{r}{R_c} \right)^2 \right)^{-1}, \quad (1)$$

where ρ is the dark matter density at radius r . In practice, the maximum velocity of the halo is fit rather than the central density:

$$V_{halo}^2(r) = V_H^2 \left[1 - \frac{R_c}{r} \arctan \left(\frac{r}{R_c} \right) \right], \quad (2)$$

where V_{halo} is the contribution of the halo to the gravitational potential at a radius r and V_H is the asymptotic velocity, equal to $\sqrt{4\pi G \rho_o R_c^2}$.

To determine the parameters of the dark matter halo, the derived rotation curves were fit using a maximum-disk method. In this method, the disk mass-to-light ratio is fit using the inner part of the rotation curve without overshooting the derived circular velocities. Initially, the maximum mass-to-light ratio (in the B-band) is found by assuming no dark matter is present. For the warped disk model, the rotation curve derived from only the observable mass rapidly underestimated the observed rotation curve at large radii. Thus, the presence of a dark matter halo was assumed and the dark matter halo core radius, maximum velocity, and disk mass-to-light ratio were fit in an iterative manner. In contrast, the falling rotation curve model was well fit by the luminous matter alone and did not require a dark matter halo (i.e., the falling rotation curve is nearly Keplerian in nature). The derived rotation curve decompositions are shown in Figure 7. In both cases, the derived disk mass-to-light ratios (3.0 for a warped disk, 3.7 for a falling rotation curve) are reasonable for the observed colors (see, e.g., Broeils 1992).

One significant difference between the two models is the derived dynamical mass. For a spherical mass distribution, the dynamical mass within radius r is:

$$M_T(r) = 2.326 \times 10^5 V^2(r) r \quad (3)$$

where $V(r)$ is in km s^{-1} and r is in kpc. However, if no dark matter halo is required, the system is disk-like and the dynamical mass is significantly less than that calculated assuming a spherical

halo. For the falling rotation curve model, the dynamical mass is simply the sum of the gaseous and stellar mass, $1.83 \times 10^{11} M_{\odot}$. For the warped disk model, the dark matter halo dominates at large radii, so the dynamical mass is given by the above equation, $4.36 \times 10^{11} M_{\odot}$ at the last measured point of the rotation curve. This latter value gives a dark-to-luminous ratio of 1.9, quite typical of Sc galaxies (Broeils 1992).

3.3. Line Shapes and Velocity Dispersion

As mentioned in Section 2, interactive Gaussian fitting was used to determine the velocity dispersion throughout the galaxy. Both the second moment map and the velocity dispersion map from GAUFIT showed an apparent trend in the velocity dispersion as a function of radius, with the inner regions of the galaxy having extremely high velocity dispersions. Despite the relatively low inclination of this galaxy, however, the velocity dispersion measurements are significantly contaminated by rotational broadening throughout the galaxy. For instance, for beams between 40 and 120 arcsec from the center, the average rotational gradient is $0.3 \text{ km s}^{-1} \text{ arcsec}^{-1}$; for beams between 210 and 300 arcsec, the average rotational gradient is $-0.2 \text{ km s}^{-1} \text{ arcsec}^{-1}$. With a $40''$ beam, this corresponds to a minimum of 8 km s^{-1} of rotational broadening per beam. Only in the outer regions of the galaxy is the velocity gradient sufficiently shallow to permit detailed analysis of the line shape and width. A line profile from gas in the outer disk is shown in Figure 8. This profile was created by averaging line profiles from regions on the eastern and western sides of the galaxy with radii between $200''$ and $260''$. The profile is well fit by a Gaussian with a velocity dispersion of 10.0 km s^{-1} .

Despite the large rotational gradient, it is possible to investigate radial trends in the velocity dispersion by deconvolving the rotational and turbulent motions. The contribution from rotational broadening can be calculated either from a rotation curve model (e.g., Table 3), or from the observed rotational gradient, as measured in the position–velocity diagram. The latter method is more direct, but is limited to regions along the major axis. However, the major axis is also the region where the rotational broadening is minimized; therefore, in the following analysis we limited our study to two independent slices $\pm 24''$ from the major axis of the high resolution data cube. The velocity dispersion was measured interactively for each beam averaged region and the rotational gradient for each region was obtained directly from the position–velocity diagram. Figure 9 shows the results of the deconvolution of thermal and rotational broadening; each slice has been folded so that all radii are positive. The observed line widths were corrected for rotational broadening by assuming that the rotational and thermal components add in quadrature. As illustrated in Figure 9, the velocity dispersion is approximately constant as a function of radius, with an average value of $9.9 \pm 1.8 \text{ km s}^{-1}$. This is in remarkably good agreement with the velocity dispersion measured from the average of profiles in the outer regions of the galaxy.

Similar results were also obtained from more detailed rotational models. An estimate of the rotational broadening throughout the disk was obtained by creating a model system with the

GIPSY task GALMOD; the system was assumed to have a negligible intrinsic velocity dispersion and the observed gas distribution and the derived (no warp) rotation curve were given as the input parameters. The derived velocity dispersion of this model system is thus indicative of the rotational broadening at any given position in the galaxy. The intrinsic velocity dispersion was recovered by subtracting, in quadrature, the model dispersion from the observed velocity dispersion of the high resolution data cube (pixel-by-pixel). Similar to the above method, no radial trend was seen in the final velocity dispersion map. The average velocity dispersion was measured to be $10.3 \pm 1.7 \text{ km s}^{-1}$ throughout the gas disk using this technique.

4. Discussion

The observed velocity dispersion is much higher than one might expect for thermal motions. For thermal broadening at 21 cm, the velocity dispersion is related to the thermal temperature by:

$$T \sim 121 \sigma_v^2. \quad (4)$$

Thus, a velocity dispersion of 9.9 km s^{-1} corresponds to a Doppler temperature of $\sim 11900 \text{ K}$, which is significantly higher than the expected temperature of the warm neutral medium (c.f. Kulkarni & Heiles 1988). However, similarly high velocity dispersions have been observed in several other galaxies (e.g., NGC 3938, van der Kruit & Shostak 1982; NGC 1058, Dickey *et al.* 1990; NGC 6946, Boulanger & Viallefond 1992; M101, Kamphuis 1993). Since neither the previous nor the present observations have adequate spatial resolution to resolve individual HI clouds, the observed velocity dispersion is the ensemble average of several clouds per beam. In fact, the mean motions of the gas clouds, rather than the temperature of the gas within each cloud, could be the dominant motion resulting in the broad velocity dispersion.

For a galaxy with a high star formation rate, turbulent motion is obviously a significant contributor to the velocity dispersion in the inner regions of the galaxy, where supernovae and outflows provide large amounts of kinetic energy. One difficulty, however, is to explain how such high levels of turbulence are sustained throughout the gas disk, particularly in regions well beyond the optical edge or in systems with modest star formation rates (such as NGC 1232). Recently, Sellwood & Balbus (1999) proposed that MHD instabilities in the differentially rotating gas disk could support a moderate amount of turbulence at all radii via dynamical heating of the disk. Their model requires a modest magnetic field ($\sim 3 \mu\text{G}$) to reproduce a velocity dispersion of 6 km s^{-1} in the outer gas disks of spiral galaxies. While it is still unclear whether this mechanism is the dominant source of turbulence at large radii, it is an intriguing possibility.

Several studies report a radial decrease in the velocity dispersion, with the outer regions of a galaxy having narrower and more perfectly Gaussian line shapes (e.g., NGC 6946, Boulanger & Viallefond 1992; M101, Kamphuis 1993). As discussed previously, NGC 1232 also has an observable radial decrease in the velocity dispersion, all of which can be accounted for by rotational broadening in the presence of a steeply rising rotation curve. While most studies acknowledge the

complications of rotational broadening, it can be quite difficult to account fully for its effects on the data. For instance, when convolved with a decreasing gas density in the center of the galaxy, beam smearing can result in highly asymmetric, non-Gaussian spectra. A velocity dispersion measured either by moment analysis or Gaussian fitting will not accurately reflect the width of the line in such spectra. Thus, it is extremely difficult to study the profile shape and radial trends in the velocity dispersion unless the observations are obtained with high spectral *and* spatial resolution.

5. Conclusions

We have investigated the gas distribution and kinematics of the nearly face-on spiral galaxy NGC 1232. Our results and conclusions are summarized below.

(1) As is typical of spiral galaxies, the neutral gas distribution extends a factor of 1.6 beyond the optical radius. The gas distribution is slightly asymmetric, with a higher gas column density associated with the prominent spiral arms on the eastern side.

(2) The observed rotation curve has a nearly Keplerian decline beyond the edge of the optical disk. Small variations in the inclination angle (which is poorly constrained due to the low inclination of this galaxy) can recover a flat rotation curve for the system. Assuming that the system is indeed warped, the dark-to-luminous ratio is 1.9.

(3) The presence of a steeply rising rotation curve complicates measurements of the velocity dispersion as a function of radius. Nonetheless, after correcting for rotational broadening, the velocity dispersion appears to be constant throughout the galaxy, with an average value of $9.9 \pm 1.8 \text{ km s}^{-1}$.

As mentioned in the introduction, one of the reasons for looking at the gas distribution of NGC 1232 was to see if there were unusual gas kinematics associated with the outermost HII regions. There are no obviously disturbed kinematic features in the present data set, but such features may have been washed out by the poor spatial resolution of the observations. Nonetheless, to first order, the spectra are all well fit by a single Gaussian (with the exception of the central region where the rotational broadening is severe) and are consistent with a slightly warped, differentially rotating, gas disk extending well beyond the optical radius. Thus, it is unlikely that large scale kinematic peculiarities are the cause of the abnormal abundances measured in the outer HII region.

Analysis of this data set emphasizes the need for good quality high resolution (both spectral *and* spatial) observations of face-on galaxies. The few canonical systems (e.g., NGC 1058 and NGC 3938) have been studied extensively with both WSRT and the VLA, but more systems are needed to address possible dependences of the velocity dispersion on galaxy morphology and star formation rates. While the requirement for low inclination angles significantly restricts the

potential target list, corrections for rotational broadening are less important with high spatial resolution observations. In fact, these studies will become more feasible within the next few years; with a new correlator, the upgraded VLA will permit high velocity resolution over a wide bandpass, thereby improving the quality of similar observations of moderately inclined spiral galaxies.

We thank the NRAO summer students of 1992 who elected to observe NGC 1232 as part of their summer student project: Chris De Pree, Robbie Dohm–Palmer, Eric Olson, Ben Oppenheimer, Carlos Rabaca, James Sweeney, and Eric Wagoner. We thank Michael Rupen, Katrina Koski, Andreea Petric, and Dave Westpfahl for many informative conversations about gas in face-on galaxies. Martha Haynes kindly provided access to the Palomar 5m telescope for the redshift determination of N1232A. We thank the anonymous referee for thoughtful comments on rotational broadening. Robbie Dohm–Palmer and Katrina Koski are gratefully acknowledged for providing helpful comments on an early draft of the paper. JB acknowledges funding through the Research Experience for Undergraduates program run by the NRAO and funded by the National Science Foundation.

A. Metallicity of NGC 1232A

As noted in Section 2, optical spectra of NGC 1232A were obtained with the Palomar 5m telescope during the night of 1999 January 23. The spectra were of sufficient quality that further analysis (beyond the redshift determination) was warranted. Here, we describe the observations in more detail and present the results of oxygen and nitrogen abundance calculations for the two HII regions observed.

During the observations, a long slit ($2'$) with a $2''$ aperture was centered on NGC 1232A for one 1200 sec exposure. The slit was positioned at an angle of 0° (the parallactic angle at the time of the observation) and passed through both the center of the galaxy and an HII region $19''$ to the south (Figure 10). A 5500 \AA dichroic was used to split the light to the two sides (blue and red), providing complete spectral coverage from $3600\text{--}7600 \text{ \AA}$. The blue spectra were acquired with the 600 lines/mm diffraction grating (blazed at 4000 \AA). The red spectra were acquired with the 316 lines/mm diffraction grating (blazed at 7500 \AA). Thinned 1024×1024 Tek CCDs, with read noises of $8.6 e^-$ (blue) and $7.5 e^-$ (red), were used on the two sides of the spectrograph. Both CCDs had a gain of $2. e^-/\text{DN}$. The effective spectral resolution of the blue camera was 5.0 \AA ($1.72 \text{ \AA}/\text{pix}$); the effective spectral resolution of the red camera was 7.9 \AA ($2.47 \text{ \AA}/\text{pix}$). The spatial scale of the long slit was $0.62''/\text{pix}$ on the blue and $0.48''/\text{pix}$ on the red side.

While the night was non-photometric, relative flux calibration was obtained by observations of standard stars from the list of Oke (1990). Wavelength calibration was obtained by observations of arc lamps taken before and after the galaxy observations. A Hollow Cathode (Fe and Ar) lamp

was used to calibrate the blue spectra; a combination of He, Ne, and Ar lamps were used to calibrate the red spectra.

The spectra were reduced and analyzed with the IRAF⁶ package. The spectral reduction included bias subtraction, scattered light corrections, and flat fielding with both twilight and dome flats. The 2-dimensional images were rectified based on the arc lamp observations and the trace of stars at different positions along the slit. The sky background was removed from the 2-dimensional images by fitting a low order polynomial along each row of the spectra. One dimensional spectra of the two HII regions were extracted from the rectified images using a 3.6'' extraction region for the southern HII region and a 3.0'' region for the central HII region (Figure 10). Reddening corrected line strengths for both HII regions are listed in Table 4.

Derivation of the oxygen abundance for both HII regions followed the methods described in van Zee *et al.* (1998b). The temperature sensitive line [OIII] λ 4363 was detected in the southern HII region and thus the electron temperature could be determined directly; for this HII region, the oxygen abundance was calculated using the emissivity coefficients from a version of the FIVEL program (De Robertis *et al.* 1987) assuming a low density (100 cm^{-3}) and a T_e of $11050 \pm_{1210}^{2530}$. For the central HII region, the oxygen abundance was estimated based on the strong line ratios ($R_{23} \equiv ([\text{OII}] + [\text{OIII}])/\text{H}\beta$) using the model grid of McGaugh (1991). An electron temperature of 6500 ± 500 K reproduced this estimated oxygen abundance, and was thus adopted to derive the N/O ratio for the HII region. The derived oxygen and nitrogen abundances for both HII regions are listed in Table 4. Not unexpectedly, the southern HII region is relatively low abundance while the central HII region is significantly higher abundance. With measurements of only two HII regions in hand, the derivation of an abundance gradient in this system is premature; nonetheless, to first order, the abundance gradient is similar to those found in other spiral galaxies (e.g., Vila-Costas & Edmunds 1992; Zaritsky *et al.* 1994; van Zee *et al.* 1998b).

REFERENCES

- Becker, R., Mebold, U., Reif, K., & van Woerden, H. 1988, A&A, 203, 21
Boulanger, F., & Viallefond, F. 1992, A&A, 266, 37
Briggs, D. 1995, PhD Thesis, New Mexico Tech
Brinks, E., & Bajaja, E. 1986, A&A, 169, 14
Broeils, A. H. 1992, PhD thesis, University of Groningen
Broeils, A. H., & Rhee, M.-H. 1997, A&A, 324, 877
Broeils, A. H., & van Woerden, H. 1994, A&AS, 107, 129
Cayatte, V., Kotanyi, C., Balkowski, C., & van Gorkom, J. H. 1994, AJ, 107, 1003

⁶IRAF is distributed by the National Optical Astronomy Observatories.

- Condon, J. J. 1987, *ApJS*, 65, 485
- de Jong, R. S. 1996, *A&A*, 313, 377
- De Robertis, M. M., Dufour, R. J., & Hunt, R. W. 1987, *JRASC*, 81, 195
- de Vaucouleurs, G., de Vaucouleurs, A., Corwin, H. G., Buta, R., Paturel, G., & Fouqué, P. 1991, *Third Reference Catalogue of Bright Galaxies* (Springer, New York) (RC3)
- Dickey, J. M., Hanson, M. M., & Helou, G. 1990, *ApJ*, 352, 522
- Fisher, J. R. & Tully, R. B. 1981, *ApJS*, 47, 139
- Ferguson, A. M. N., Gallagher, J. S., & Wyse, R. F. G. 1998a, *AJ*, 116, 673
- Ferguson, A. M. N., Wyse, R. F. G., Gallagher, J. S., & Hunter, D. A. 1998b, *ApJ*, 506, L19
- Haynes, M. P., Hogg, D. E., Maddalena, R. J., Roberts, M. S., & van Zee, L. 1998, *AJ*, 115, 62
- Jore, K. P., Broeils, A. H., & Haynes, M. P. 1996, *AJ*, 112, 438
- Kamphuis, J. 1993, PhD thesis, University of Groningen
- Kamphuis, J., & Briggs, F. 1992, *A&A*, 253, 335
- Kulkarni, S. R., & Heiles, C. 1988, in *Galactic and Extragalactic Radio Astronomy*, G.L. Verschuur and K.I. Kellermann, eds., (Springer-Verlag: New York)
- McCall, M. L., Rybski, P. M., & Shields, G. A. 1985, *ApJS*, 57, 1
- McGaugh, S. S. 1991, *ApJ*, 380, 140
- Napier, P. J., Thompson, R. T., & Ekers, R. D. 1983, *Proc. IEEE*, 71, 1295
- Oke, J. B. 1990, *AJ*, 99, 1621
- Reif, K., Mebold, U., Goss, W. M., van Woerden, H., & Siegman, B. 1982, *A&AS*, 50, 451
- Roberts, M. S., & Haynes, M. P. 1994, *ARA&A*, 32, 115
- Rownd, B. K., Dickey, J. M., & Helou, G. 1994, *AJ*, 108, 1638
- Sellwood, J. A., & Balbus, S. A. 1999, *ApJ*, 511, 660
- Shostak, G. S., & van der Kruit, P. C. 1984, *A&A*, 132, 20
- Soifer, B. T., Boehmer, L., Neugebauer, G. & Sanders, D. B. 1989, *AJ*, 98, 766
- Sparke, L. S., & Casertano, S. 1988, *MNRAS*, 234, 873
- Staveley-Smith, L., & Davies, R. D. 1988, *MNRAS*, 231, 833
- van der Hulst, J. M., Terlouw, J. P., Begemen, K., Zwitser, W., & Roelfsema, P. R. 1992, in *Astronomical Data Analysis Software and Systems*, ed. D. Worall, C. Biemesderfer, and J. Barnes (ASP Conference Series), 25, 131
- van der Kruit, P. C., & Shostak, G. S. 1982, *A&A*, 105, 351
- van der Kruit, P. C., & Shostak, G. S. 1984, *A&A*, 134, 258

van Zee, L., Salzer, J. J., & Haynes, M. P. 1998a, *ApJ*, 497, L1

van Zee, L., Salzer, J. J., Haynes, M. P., O’Donoghue, A. A., & Balonek, T. J. 1998b, *AJ*, 116, 2805

Vila-Costas, M. B., & Edmunds, M. G. 1992, *MNRAS*, 259, 121

Zaritsky, D., Kennicutt, R. C., & Huchra, J. P. 1994, *ApJ*, 420, 87

This preprint was prepared with the AAS L^AT_EX macros v4.0.

Table 1. Physical Properties of NGC 1232

Parameter	Value
Distance (Mpc)	21.5 ^a
Kinematic Center (B1950)	03 07 30.2, –20 46 08
HI Properties:	
Integrated H I flux density (Jy km s ^{–1})	122.4 ± 12.2
Heliocentric velocity (km s ^{–1})	1678.9 ± 1.0
H I profile width (50%) (km s ^{–1})	234 ± 2.
H I profile width (20%) (km s ^{–1})	256 ± 3.
Velocity Dispersion (km s ^{–1})	9.9 ± 1.8
H I size at 10 ²⁰ atoms cm ^{–2} (arcmin × arcmin)	11.6 × 9.7
Peak H I surface density (atoms cm ^{–2})	1.4 × 10 ²¹
Optical Properties:	
Apparent blue magnitude	10.52 ± 0.14 ^b
(U–B) ₀	–0.02 ± 0.10 ^b
(B–V) ₀	0.60 ± 0.04 ^b
R ₂₅ (kpc)	23.2 ^b
R _d (kpc)	6.3 ^a
Derived Properties:	
Hydrogen mass, M_{HI} (10 ¹⁰ M_{\odot})	1.33
Optical luminosity, L_{B} (10 ¹⁰ L_{\odot})	4.46
FIR luminosity, L_{FIR} (10 ¹⁰ L_{\odot})	0.875 ^c
Dynamical mass, M_{T} (10 ¹⁰ M_{\odot})	43.6
Dynamical mass – no warp, M_{T} (10 ¹⁰ M_{\odot})	18.3
$M_{\text{HI}}/L_{\text{B}}$ (M_{\odot}/L_{\odot})	0.3
$M_{\text{HI}}/M_{\text{T}}$	0.03
$M_{\text{dark}}/M_{\text{lum}}$	1.9

^avan Zee et al. 1998

^bde Vaucouleurs et al. 1991

^cSoifer et al. 1989

Table 2. Parameters of the HI Data Cubes

Robustness Parameter	Beam [arcsec \times arcsec]	rms [mJy beam $^{-1}$]	linear resolution [kpc beam $^{-1}$]
1	53.9 \times 26.2	1.7	5.6 \times 2.7
0.5	50.3 \times 24.0	1.7	5.2 \times 2.5
-0.5	43.2 \times 21.1	2.0	4.5 \times 2.2

Table 3. Rotation Curve of NGC 1232

radius [arcsec]	Σ_{HI} [M_{\odot} pc $^{-2}$]	i [$^{\circ}$]	PA [$^{\circ}$]	V_c [km s $^{-1}$]
10.	1.27	30	270	70.7 \pm 20.7
40.	2.20	30	270	184.9 \pm 1.4
70.	4.23	30	270	209.9 \pm 1.6
100.	5.85	30	270	216.6 \pm 0.8
130.	6.34	30	270	221.8 \pm 0.7
160.	5.91	30	270	220.1 \pm 0.6
190.	5.14	29	270	221.0 \pm 0.6
220.	3.70	28	269	220.9 \pm 0.7
250.	2.18	26	268	219.4 \pm 1.3
280.	1.19	23	268	218.8 \pm 1.7
310.	0.72	21	268	215.8 \pm 1.6
340.	0.52	20	268	219.1 \pm 1.9
370.	0.41	20	269	217.9 \pm 2.3
400.	0.32	20	269	217.8 \pm 6.4

Table 4. Optical Line Intensities for NGC 1232A

Ionic Species	Rest Wavelength	NGC 1232A (000+000) I(λ)/I(H β)	NGC 1232A (000–019) I(λ)/I(H β)
[OII]	3728	2.32 ± 0.17	2.30 ± 0.14
[NeIII]	3869	...	0.19 ± 0.02
HI	4340	0.47 ± 0.05	0.47 ± 0.03
[OIII]	4363	...	0.037 ± 0.016
HI	4861	1.00 ± 0.06	1.00 ± 0.05
[OIII]	4959	0.61 ± 0.05	1.34 ± 0.06
[OIII]	5007	1.81 ± 0.11	4.33 ± 0.19
HeI	5876	0.09 ± 0.01	0.10 ± 0.01
[OI]	6300	0.09 ± 0.12	0.064 ± 0.005
[OI]	6364	0.03 ± 0.01	0.020 ± 0.003
[NII]	6584	0.11 ± 0.01	0.045 ± 0.004
HI	6563	2.86 ± 0.22	2.84 ± 0.18
[NII]	6584	0.38 ± 0.03	0.14 ± 0.01
HeI	6678	...	0.038 ± 0.004
[SII]	6716	0.53 ± 0.04	0.26 ± 0.02
[SII]	6731	0.27 ± 0.02	0.15 ± 0.01
[ArIII]	7136	...	0.079 ± 0.006
$c_{H\beta}$		0.02 ± 0.08	0.24 ± 0.06
F(H β) $\times 10^{15}$		2.05	4.98
EW(H β) [Å]		10.8	95.3
log(R ₂₃)		0.676 ± 0.019	0.902 ± 0.013
T(O ⁺⁺)		6500 ± 500	$11050 \pm_{1210}^{2530}$
12 + log(O/H)		8.79 ± 0.10	8.21 ± 0.10
log(N/O)		-1.24 ± 0.14	-1.42 ± 0.15

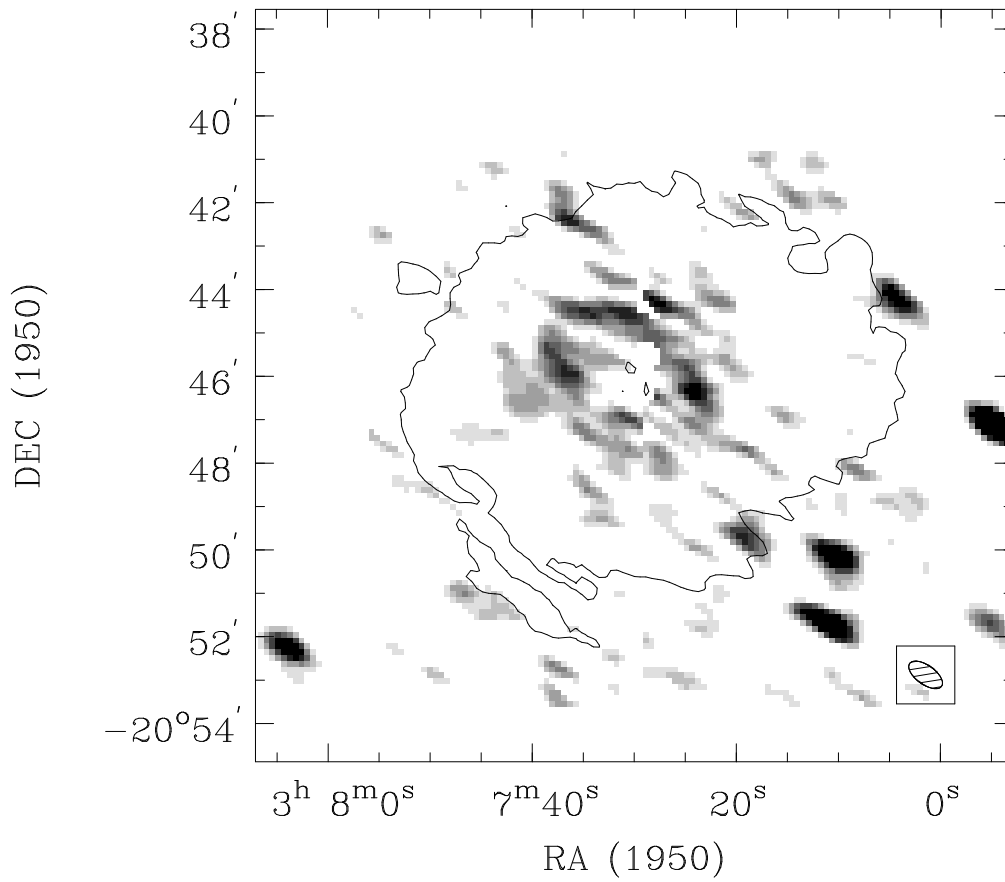


Fig. 1.— Continuum emission from the intermediate weight data cube. The beam size is 50.3×24.0 arcsec. The region of HI emission is outlined at a column density limit of 10^{20} atoms cm^{-2} . The inner ring of continuum emission is spatially coincident with the spiral arms.

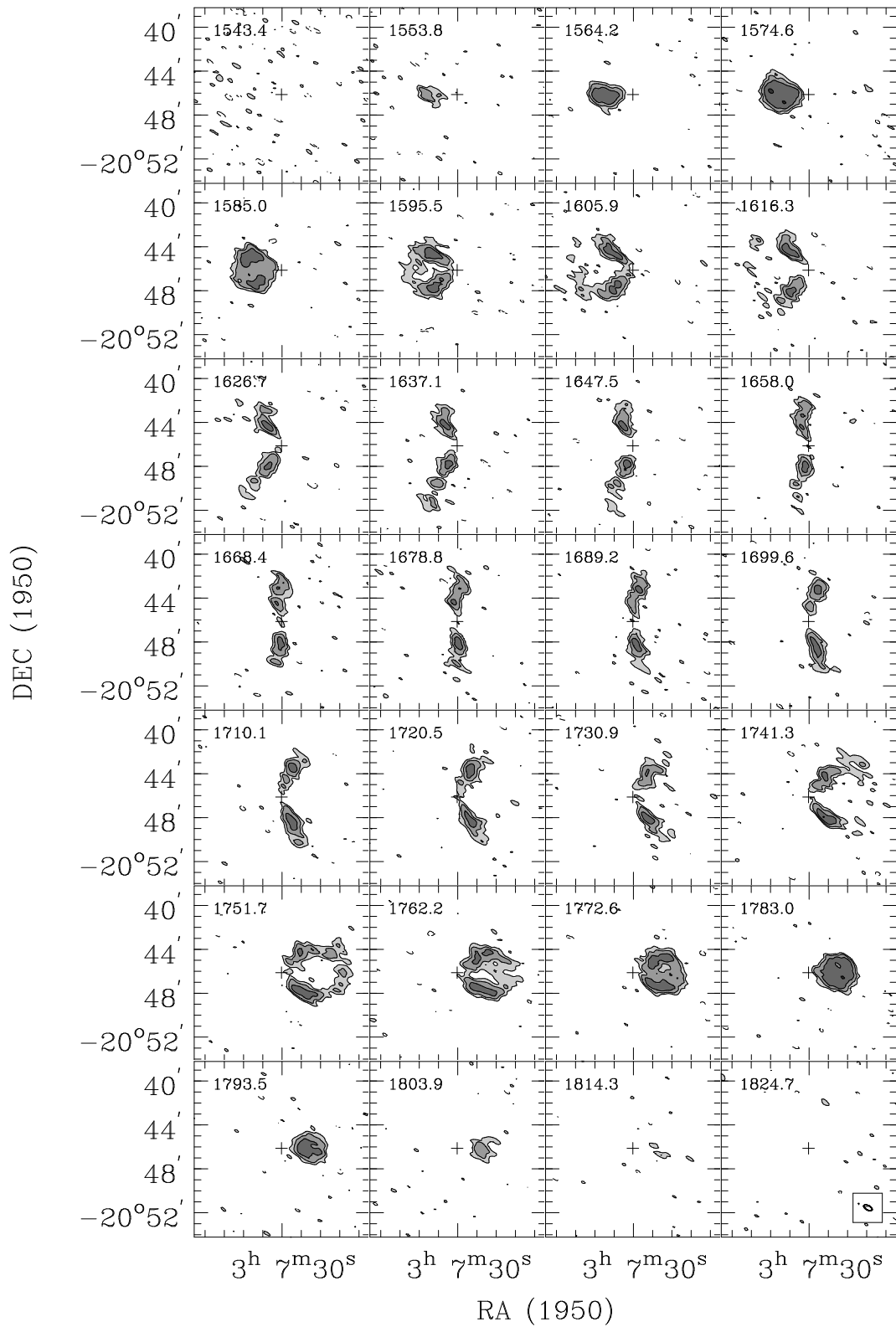


Fig. 2.— Selected channels from the intermediate weight HI data cube. Every fourth channel is shown. The beam size, illustrated in the lower right panel, is 50.3×24.0 arcsec. The contours represent -3σ , 3σ , 6σ , and 12σ . The dynamical center is marked with a cross.

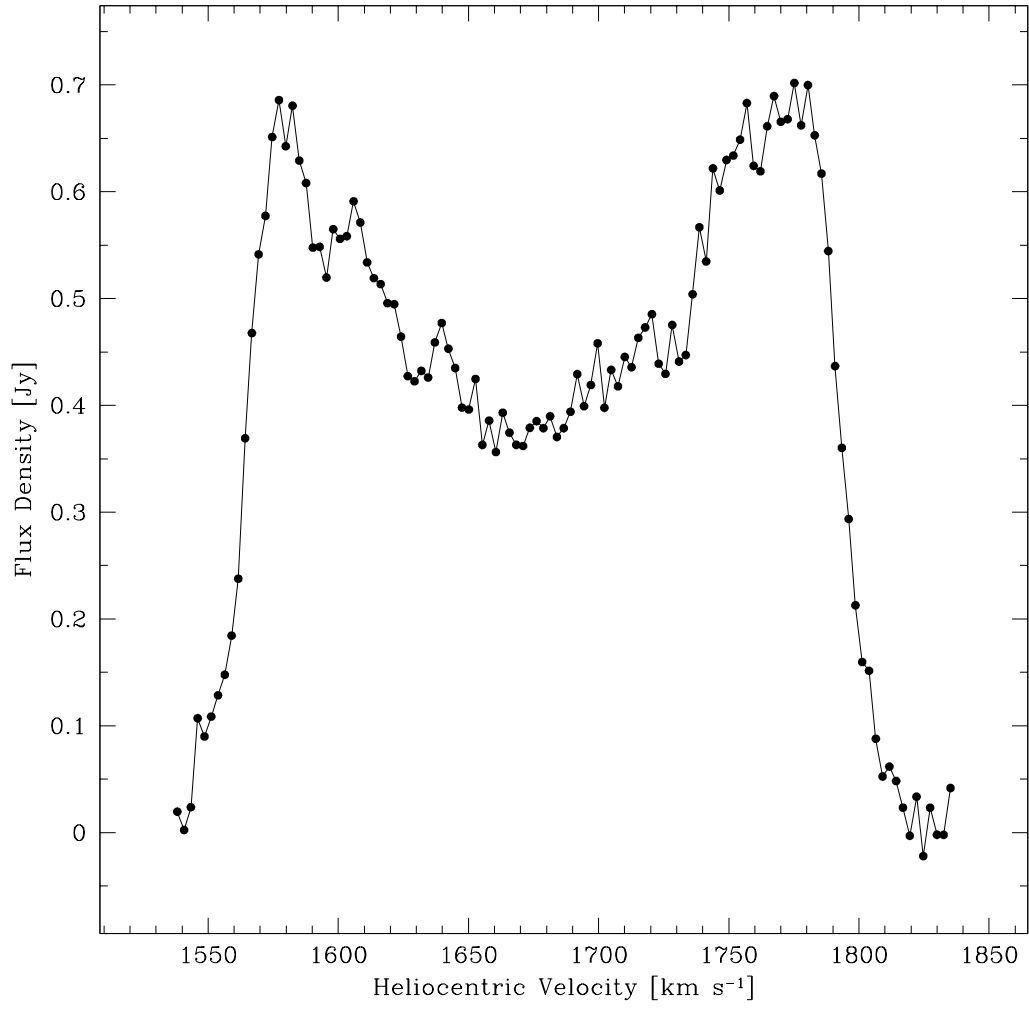


Fig. 3.— The global HI profile for NGC 1232 derived from the continuum subtracted low resolution HI data cube. The total flux density is recovered in the VLA observations.

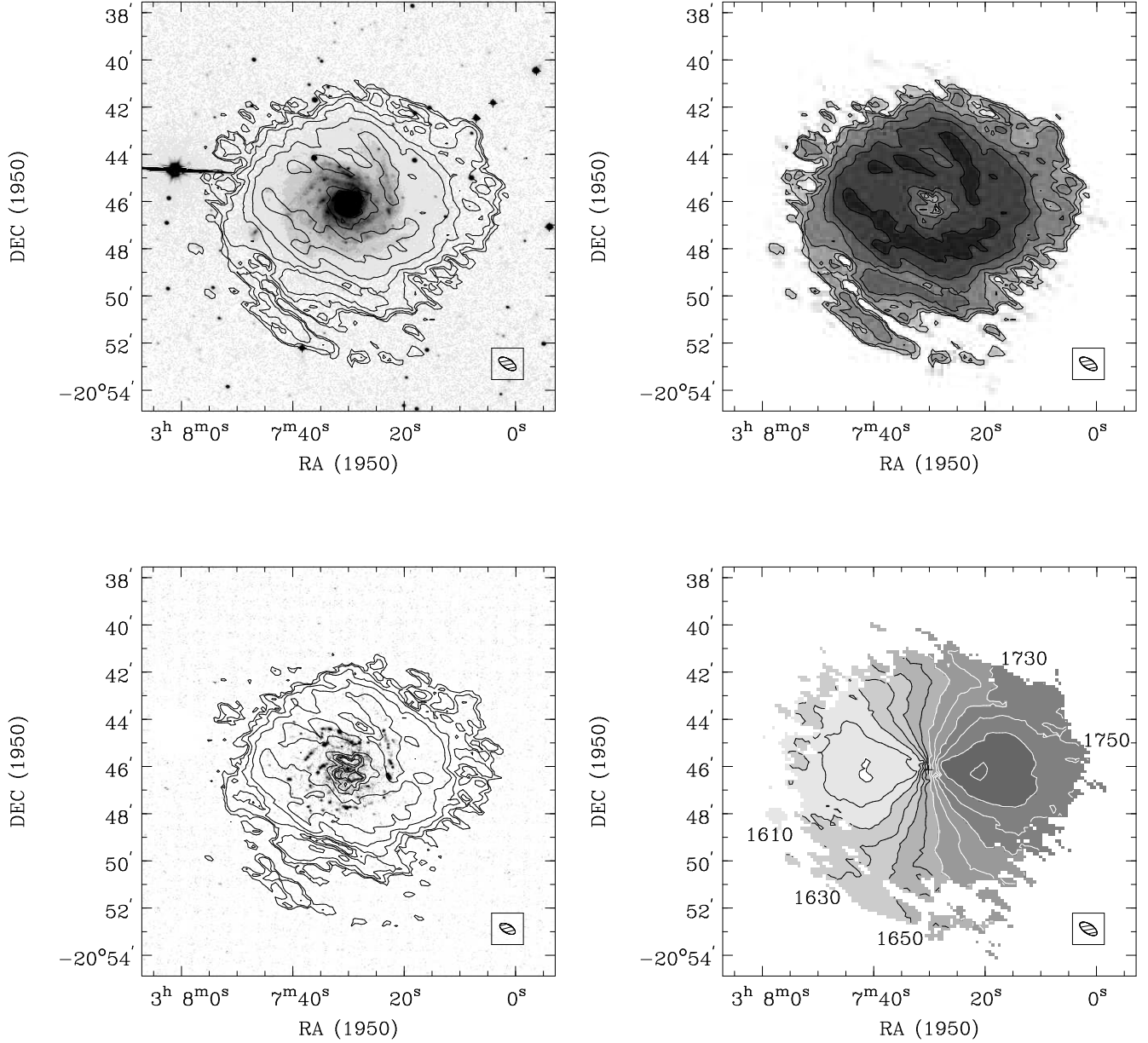


Fig. 4.— Moment maps of NGC 1232. (a) The HI contours from the intermediate weight data cube are shown overlaid on an optical R band image. The HI contours are $0.3, 0.6, 1.2, 2.4, 4.8, 9.6,$ and $19.2 \times 10^{20} \text{ cm}^{-2}$. The HI beam size is 50.4×24.0 arcsec. The pixel scale of the optical image is $2.03 \text{ arcsec pixel}^{-1}$. (b) Same as (a) but with the HI column density distribution in both grey scale and contours. (c) The HI contours from the high resolution data cube overlaid on an H α image. The HI contours are $0.5, 1, 2, 4,$ and $8 \times 10^{20} \text{ atoms cm}^{-2}$ with a beam size of 43.2×21.1 . The pixel scale of the H α image is $2.03 \text{ arcsec pixel}^{-1}$. (d) The velocity field of the intermediate weight data cube. The contours are marked every 20 km s^{-1} .

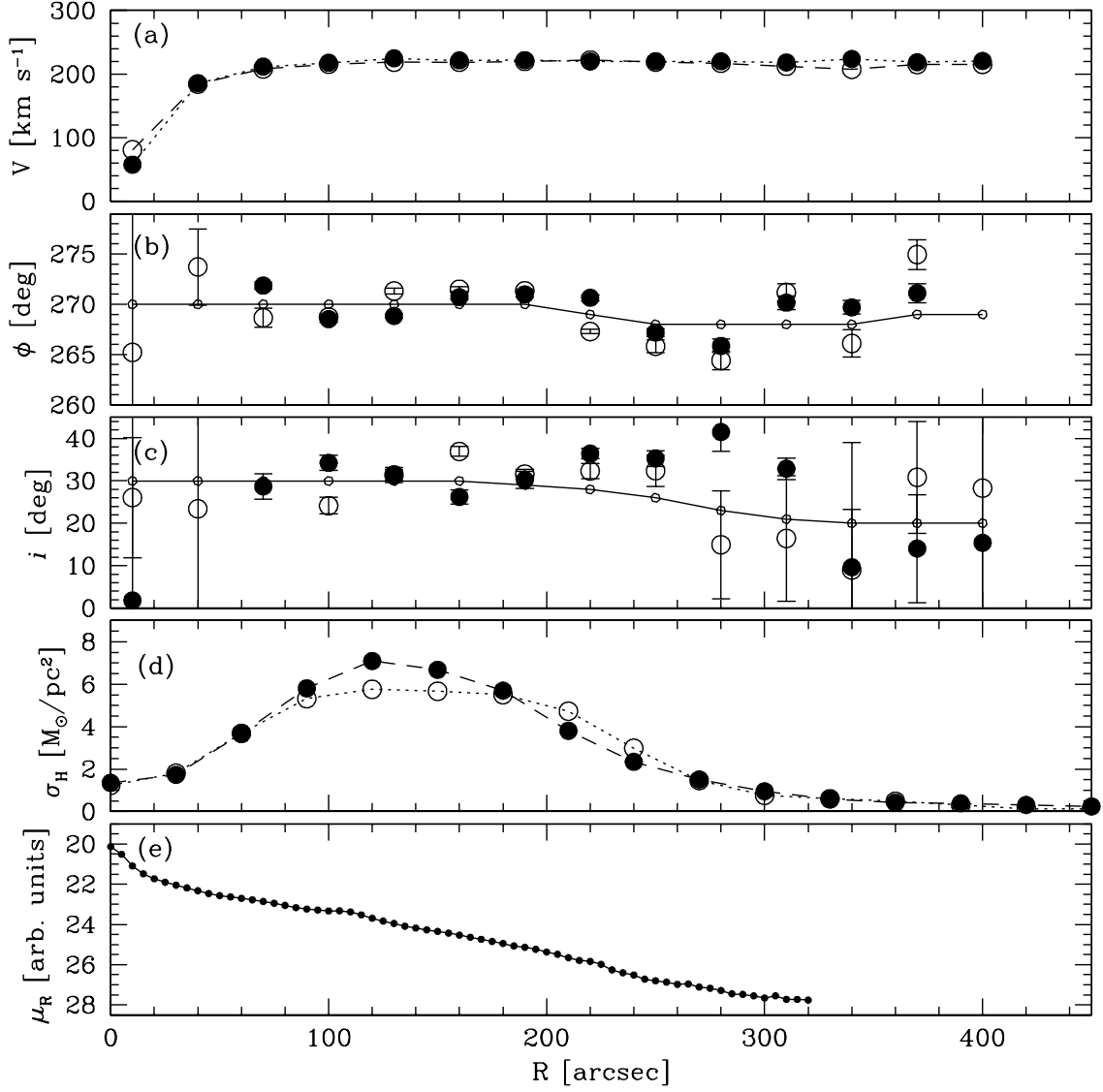


Fig. 5.— Rotation curve fitting parameters: (a) the derived rotation curve, (b) position angle, (c) inclination angle, (d) neutral gas surface density, and (e) optical surface brightness. The rotation curve was fit in GIPSY using an iterative process. The approaching (eastern) and receding (western) sides are represented by filled and open circles, respectively. The values used to derive the rotation curve are indicated by the connected points. The R-band optical surface brightness is displayed in arbitrary units since the image was taken under non-photometric conditions.

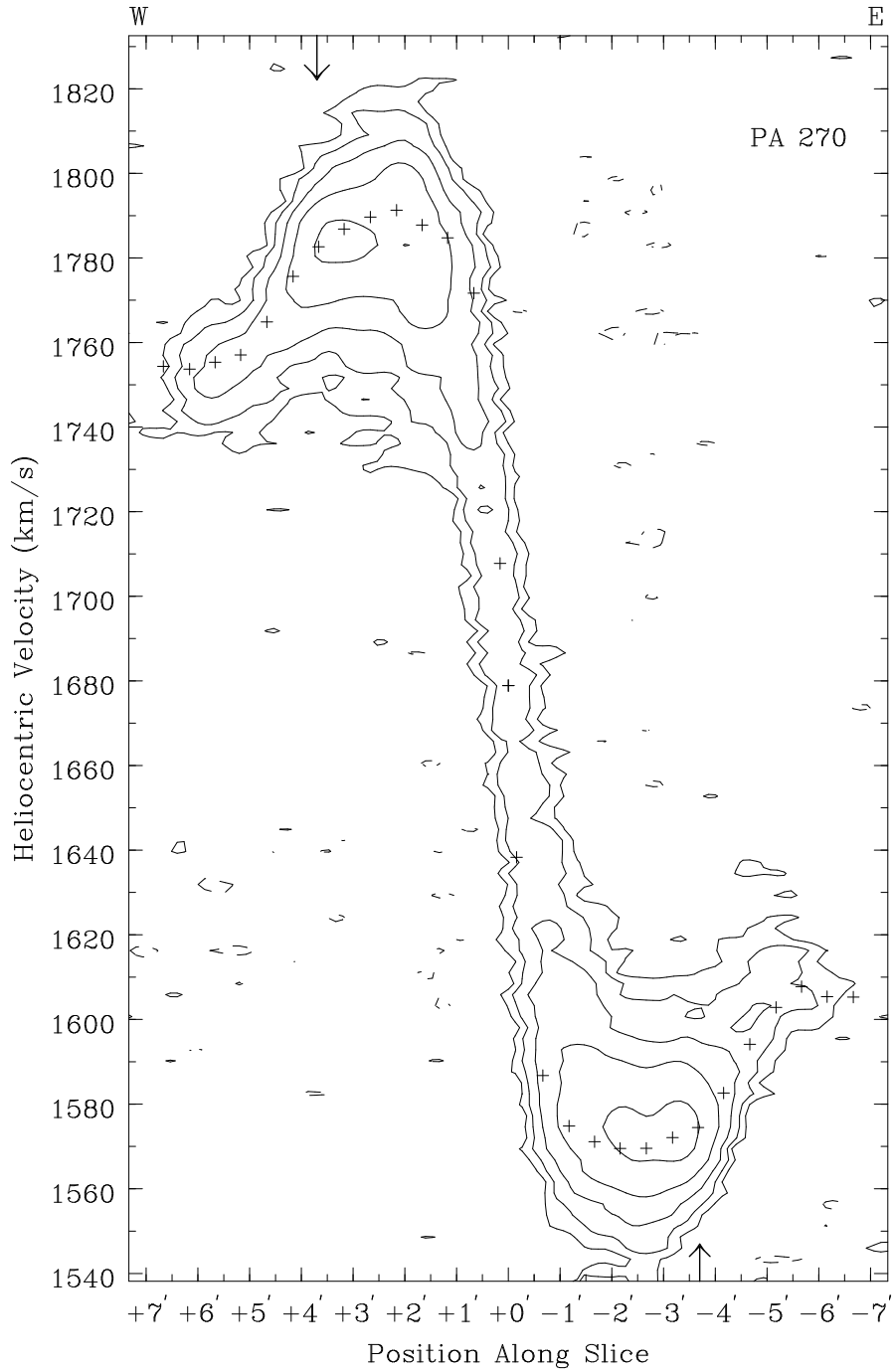


Fig. 6.— A position-velocity diagram cut at a position angle of 270° . The derived rotation curve is marked by crosses. Radii corresponding to R_{25} are denoted by arrows. The observed falling rotation curve has been modeled here as a warp, although other interpretations are possible.

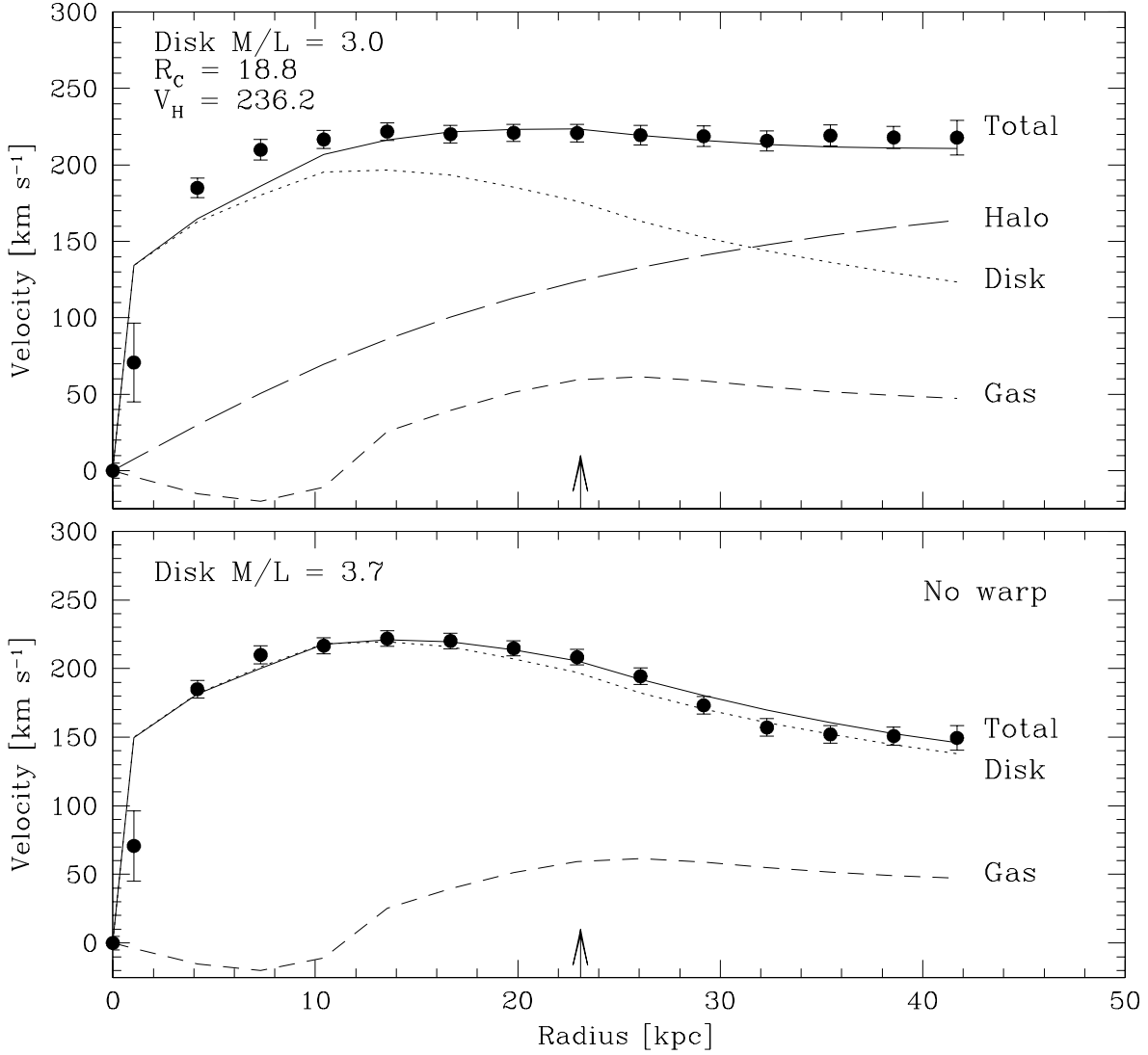


Fig. 7.— Maximum disk rotation curve decomposition. The upper panel shows the rotation curve derived by using the parameters shown in Figure 5. The lower panel shows the rotation curve derived by assuming a constant inclination of 30°. In both these panels, the total rotation curve (solid line) is the quadrature sum of the mass contributions of the stellar and gaseous disks and the dark matter halo. Note that in the inner regions, the mass distribution of gaseous disk results a net acceleration outwards (denoted by a negative velocity in these plots). The radius corresponding to R₂₅ is denoted by an arrow.

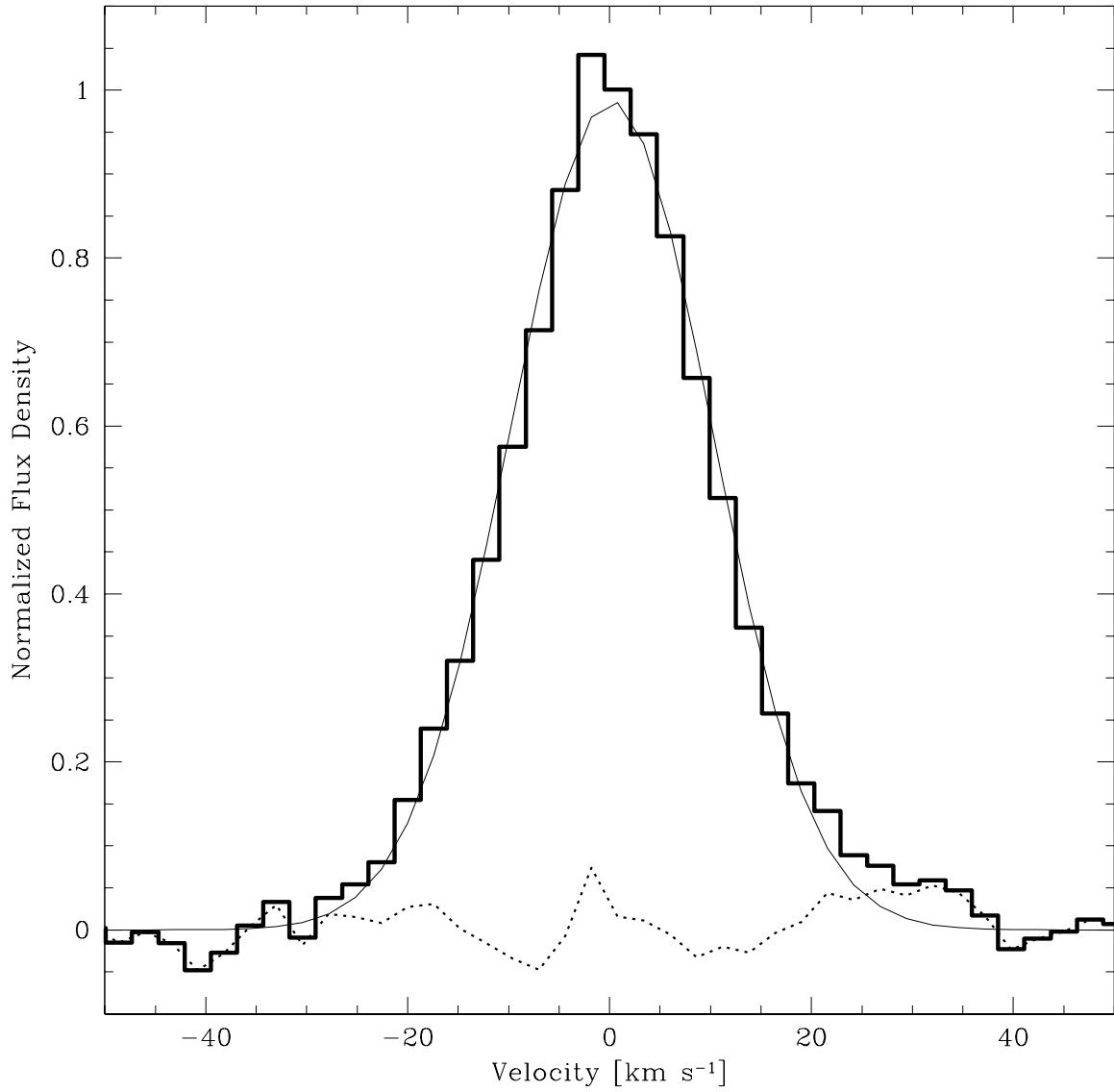


Fig. 8.— The average line profile of emission from the eastern and western sides of NGC 1232 (histogram). The line profile is well fit by a Gaussian with a velocity dispersion of 10.0 km s^{-1} (thin solid line).

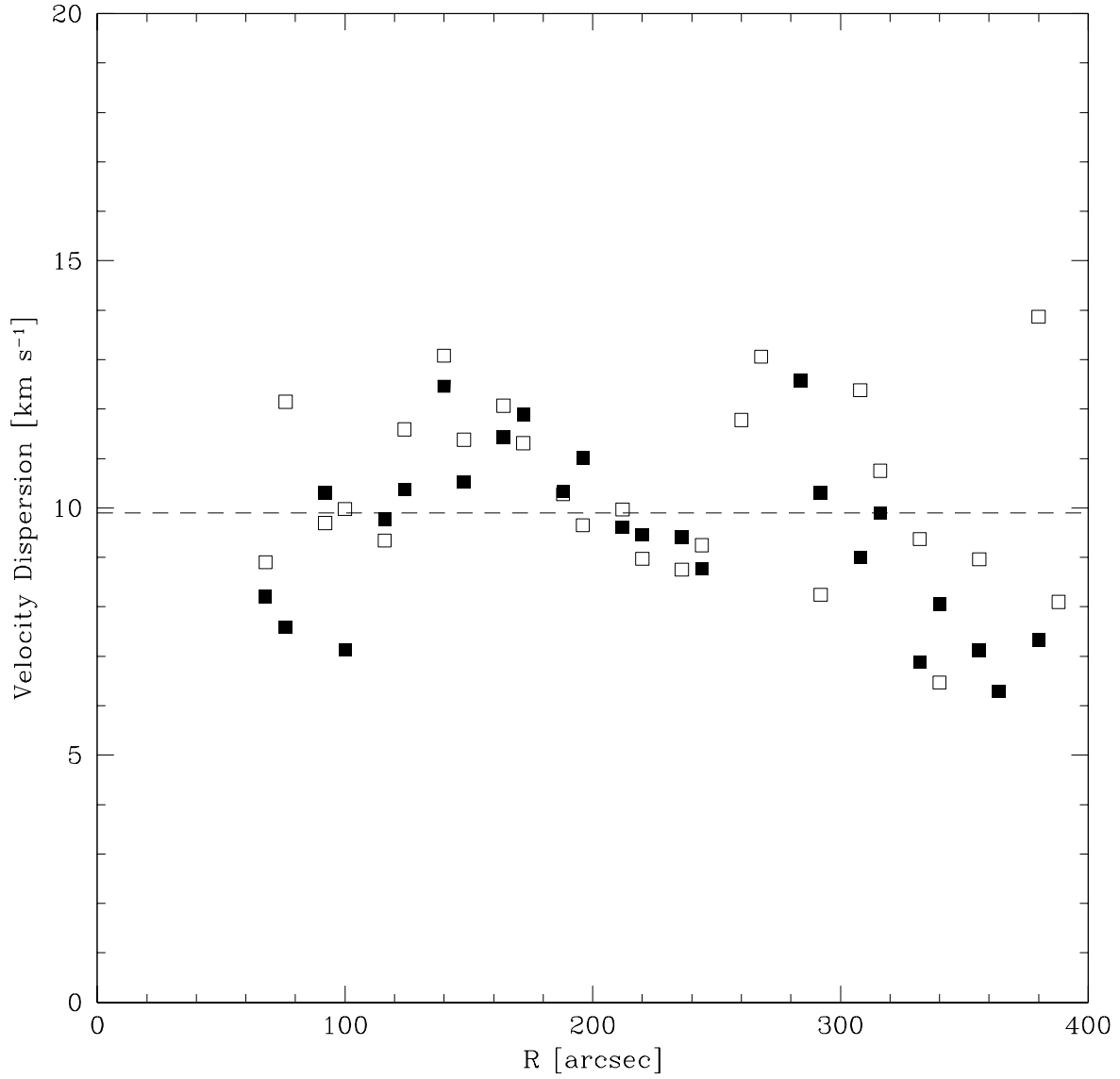


Fig. 9.— The velocity dispersion as a function of radius. The velocity dispersion was measured for spectra along two tracks parallel to the major axis of NGC 1232 (denoted by open and filled data points). There is no indication of a velocity dispersion fall off with radius. The dotted line indicates the calculated average of all the data points, $9.9 \pm 1.8 \text{ km s}^{-1}$.

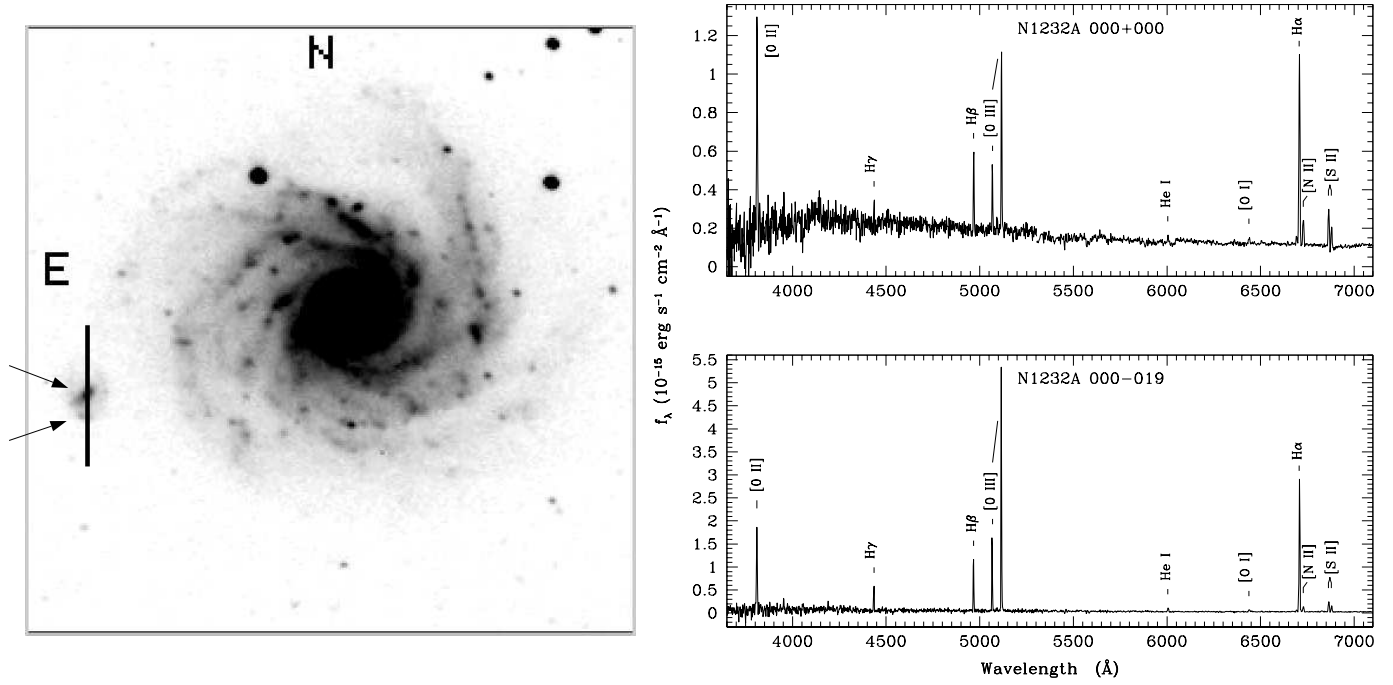


Fig. 10.— (left) R-band image of NGC 1232 and NGC 1232A showing the location of the long slit. (right) Optical spectra of the two HII regions observed in NGC 1232A. The major lines are marked.